

Evaluating Interfacial Stability in Solid-State Pouch Cells Via Ultrasonic Imaging

Yunhui Huang (✉ huangyh@hust.edu.cn)

Huazhong University of Science and Technology <https://orcid.org/0000-0003-1687-1938>

Hanyu Huo

Institute of New Energy for Vehicles, School of Materials Science and Engineering, Tongji University

Kai Huang

Huazhong University of Science and Technology

Wei Luo

Tongji University <https://orcid.org/0000-0002-4019-4634>

Jintao Meng

Huazhong University of Science and Technology

Liangyi Zhou

Huazhong University of Science and Technology

Zhe Deng

Huazhong University of Science and Technology

Jiayun Wen

Institute of New Energy for Vehicles, School of Materials Science and Engineering, Tongji University

Yiming Dai

Institute of New Energy for Vehicles, School of Materials Science and Engineering, Tongji University

Zhimei Huang

Huazhong University of Science and Technology

Yue Shen

Huazhong University of Science and Technology

Xiangxin Guo

Qingdao University <https://orcid.org/0000-0001-6732-3363>

Xiulei Ji

Oregon State University <https://orcid.org/0000-0002-4649-9594>

Article

Keywords: ultrasonic imaging, interfacial stability, gassing, solid-state batteries, Li metal anode

Posted Date: June 15th, 2021

DOI: <https://doi.org/10.21203/rs.3.rs-578754/v1>

License:  This work is licensed under a Creative Commons Attribution 4.0 International License.

[Read Full License](#)

Abstract

Chemical/electrochemical stability at the interfaces greatly affects the performance of solid-state batteries (SSBs). However, the interfacial behavior in SSBs remains elusive due to the subsurface nature of interfaces and the lack of proper characterization methods. Herein, ultrasonic imaging technology is employed to non-destructively investigate the interfacial stability in solid-state pouch cells. Benefiting from the high sensitivity of ultrasound to the gas/vacuum, *in-situ* ultrasonic imaging can effectively probe the inner gas release and interfacial degradation in pouch cells during long-term cycling. The safety issue of SSBs is highlighted by the flammable gas release detected in ultrasonic images. And the increased interfacial resistance either from contact loss or passivation layer growth is well distinguished. The gradual oxidation and gassing at the cathode interface are tracked by ultrasonic imaging, which leads to the capacity fading of SSBs. The ultrasonic imaging technology is demonstrated to be a powerful tool to evaluate the interfacial stability in SSBs, which can guide the rational design of interfaces and enhance the performance of SSBs.

Introduction

Li-ion batteries (LIBs) have transformed the lives of people through portable electronics, electric vehicles, and large-scale energy storage systems^{1,2}. However, it remains a challenge for LIBs to provide high energy density as well as infallible safety, particularly when Li metal is contemplated as the anode for next generation LIBs^{3,4}. To address the safety concern, a solution is to replace liquid electrolytes by solid-state electrolytes (SSEs) that are nonflammable and compatible with Li metal anode⁵⁻⁷. For any electrolytes, it is the interface between the electrolyte and the electrode that profoundly affects the performance of the batteries. Infamously, it has taken decades to understand the interfacial properties between liquid electrolytes and the electrodes, where solid-electrolyte interphase (SEI) forms over cycling⁸. For the emerging solid-state batteries (SSBs), it is indispensable to understand the evolving interfacial properties between SSEs and the electrodes during long-term cycling⁹⁻¹¹. For example, albeit sulfide-based SSEs show competitive ionic conductivities, it is believed that non-conductive behavior of the interfaces of this type of SSEs leads to low Coulombic efficiency, rapid capacity fading, and poor cycling life¹². Various strategies have been reported to enhance the interfacial stability between SSE and the Li metal anode such as the intermediate layers introduced^{13,14} and the surface impurities removed¹⁵. Yet, efforts are still in demand to further improve the interfacial stability, particularly by eliminating the loss of the SSE/Li contacts due to cyclic volumetric changes of Li metal anode. Providing solutions requires the fundamental understanding on detailed interfacial evolution process in SSBs, which remains elusive due to the subsurface nature of interfaces.

Current characterization techniques have their limitations when characterizing the interfacial changes in the SBBs. Electron microscopy techniques such as scanning electron microscopy (SEM) and transmission electron microscopy (TEM) can only see the side-view of the edge of the solid/solid interfaces and require careful sample processing¹⁶. Synchrotron-based X-ray techniques, such as X-ray

absorption near edge structure (XANES) and high-energy X-ray photoelectron spectroscopy (HEXPS), are employed to investigate the chemical/electrochemical interfacial reactions. However, X-ray techniques are not sensitive to the evolved gas or nano-scale contact loss due to the low scattering rate of X-ray. Neutron-based methods is sensitive to the light elements such as Li and H, which is powerful to probe the structure changes and the gas generation at the interface. Unfortunately, the cost of neutron source is extremely high. Therefore, it is desirable to develop novel low-cost, non-destructive, high sensitivity *in-situ* characterization methods with spatial resolution to probe early stage structural evolution at SSE/electrode interfaces in fully packaged SSBs ¹⁷⁻¹⁹.

Herein, we report for the first time to use the ultrasonic imaging technology to study the interfacial stability in SSBs (**Fig. 1**). The batteries are transparent to ultrasound that is highly sensitive to gas and vacuum. Even trace amount of gas generation or contact loss can be reflected on the ultrasonic transmission scanning image, which graphically reveals side-reactions and structural evolution at the interfaces. The method is nondestructive, fast, and applicable to practicable pouch-type cells during charge-discharge cycling ^{20,21}. As a demonstration, Li/SSE/Li and LiCoO₂/SSE/Li pouch-cells are studied with our method, and their failure mechanisms are discussed.

Results

Evaluating the chemical stability at the SSE/Li interface

Ultrasonic imaging first looked at the chemical stability of the interface between the composite SSE and Li metal. The composite SSE consists of the PEO polymer and Li_{6.4}La₃Zr_{1.4}Ta_{0.6}O₁₂ (LLZTO) particles, which shows the advantages of both polymer electrolytes and ceramic electrolytes for commercialized applications ²². It was fabricated by a blade-casting process using acetonitrile (ACN) as the solvent (abbreviated as PLLZ@BC) (**Supplementary Fig. 1a**). The PLLZ@BC shows higher ionic conductivity than the single phase PEO electrolyte due to the interfacial percolation effect (**Supplementary Fig. 2a**) ²³. Focused ultrasound beam with a diameter less than 1 mm is scanned with a position control accuracy of 0.2 mm, which leads to sub-millimeter resolution. The transmitted ultrasonic wave at each point of the sample is recorded via progressive scanning. The peak-to-peak value (PPV) of the recorded wave is subsequently transformed into colors from blue to red, creating the ultrasonic images.

As shown in **Fig. 2a**, the region of the Al laminate film appears red with a PPV of 1.18 V, while the region of the Li metal appears yellow with a decreased PPV of 0.83 V. In addition, the region of the PLLZ@BC shows a PPV of 0.58 V, corresponding to a green color (**Supplementary Fig. 3**). The results show that the ultrasonic beam does not attenuate much after penetrating Li metal and PLLZ@BC (**Fig. 2c**). In stark contrast, the ultrasound intensity decreases significantly when the Li metal is covered with a layer of PLLZ@BC, resulting in a deep blue ultrasonic image (**Fig. 2b** and **2d**). Such significant attenuation of the ultrasonic signal usually indicates the existence of gas ²⁴. When the ultrasonic wave passes through the interface of two different media, the transmission and reflection ratios can be calculated according to

the following formulas²⁵, respectively, where Z_1 and Z_2 are the acoustic impedances of the two different media.

$$\text{Transmission rate: } T = \frac{4z_1 \cdot z_2}{(z_1 + z_2)^2} \quad (1)$$

$$\text{Reflection rate: } R = \frac{(z_2 - z_1)^2}{(z_1 + z_2)^2} \quad (2)$$

According to these formulas, a high transmission rate is obtained by similar Z_1 and Z_2 , while different Z_1 and Z_2 can lead to a high reflection rate. The acoustic impedance of solid and liquid materials ranges from 1 to 50 MRayl. However, the acoustic impedance of gas is only 0.0004 MRayl. At the solid/gas interfaces, such a big difference causes more than 99.99% intensity loss of ultrasonic signals. Therefore, a small amount of gas at the Li/PLLZ@BC interface can dramatically decrease the ultrasonic transmissivity, thus rendering a blue color.

To further evaluate the gassing process, Li/PLLZ@BC/Li symmetric pouch cells (30 mm×25 mm) were assembled (**Fig. 2e**). **Fig. 2f** shows the time-dependent ultrasonic images overlapped on the cell photograph. A deep blue color is obtained at the initial time, indicating the gas release as soon as the PLLZ@BC contacts with the Li metal. Due to the continuous gas release, the blue area is gradually expanded. Since gas does not conduct ions, the interfacial resistance increases from 1.2 to 3.4 k Ω after 1 h, further confirming the deterioration of the contacts between the PLLZ@BC and Li metal (**Fig. 3a**). The released gas is analyzed with differential electrochemical mass spectrometry (DEMS), and is found to be some reductive species including H₂, CH₄, C₂H₆, and C₂H₄ (**Fig. 3b**). Note that these gases are all highly flammable, thus leading to the potential safety issue of SSBs. Therefore, it is crucial to find the source of gassing.

It is generally believed that both the LLZTO and PEO are chemically stable with the Li metal^{3,26}. We then looked into ACN, which was used during the blade-casting process. Thermogravimetric analysis (TGA) shows a weight loss of 2.8% at 300 °C, which corresponds to the residual ACN in the PLLZ@BC electrolyte (**Fig. 3c**). Along this line, we further analyze the gassing reaction between ACN and Li metal with DEMS analysis and density functional theory (DFT) calculations. Based on the detected gas molecules, the possible reactions between ACN and Li metal are proposed, and the reaction energy is calculated accordingly. **Fig. 3d** shows that the reaction energy is all negative, indicating the thermodynamic feasibility for the gas release. Moreover, the introduction of LiTFSI can promote a higher reactivity of ACN toward gas generation. LiTFSI as a common Li salt is added into the PLLZ@BC electrolyte (EO/Li⁺ = 12:1 by mol) to conduct Li⁺. To investigate the relative stability of ACN and ACN@LiTFSI, their highest occupied molecular orbital (HOMO) and the lowest unoccupied molecular orbital (LUMO) were calculated. In general, the stability window between anodic and cathodic potentials can be reflected by the energy difference between HOMO and LUMO²⁷. The energy difference for ACN is 9.89 eV, while the energy difference for ACN@LiTFSI is 7.39 eV (**Fig. 3e**). The decreased energy difference indicates the enhanced reaction reactivity when LiTFSI is introduced into the ACN to react with the Li

metal. DEMS results also show the longer time of gas generation, further confirming our hypothesis that LiTFSI improved the reactivity between the ACN and the Li metal (**Fig. 3f-3h**).

To eliminate the negative effects of residual ACN, a solvent-free hot-pressing method is employed to fabricate the composite electrolyte (**Supplementary Fig. 1b**). PEO polymer is mixed with LLZTO and LiTFSI, and then directly pressed into the SSE film at 100 °C (**Supplementary Fig. 2**)²⁸. The obtained film is abbreviated as the PLLZ@HP. The physical and electrochemical properties of PLLZ@HP and PLLZ@BC are compared in Fig. S2. PLLZ@HP exhibits a slightly lower ionic conductivity ($3.4 \times 10^{-5} \text{ S cm}^{-1}$) than PLLZ@BC ($1.1 \times 10^{-4} \text{ S cm}^{-1}$) at 25 °C, but much improved interfacial chemical stability. According to the ultrasonic transmission image, most of the battery core region exhibits green color with a PPV of 0.51, indicating modest ultrasonic transmissivity and good interfacial contact (**Fig. 4a and 4b**). Some unevenly distributed blue areas with a low PPV are also seen, indicating uneven contacts. Unlike PLLZ@BC, the ultrasonic transmission images of the Li/PLLZ@HP/Li cell remain unchanged during resting for 1.5 h, indicative of negligible gas release (**Fig. 4a**). The interfacial resistance measured by the EIS remains stable after 1.5 h (**Supplementary Fig. 4**). And no gas is detected by DEMS, which confirms the interfacial stability (**Supplementary Fig. 5**). The contact quality of the Li/PLLZ@HP/Li cell can be improved by the hot-pressing at 60 °C. As shown in **Fig. 4c**, most area of the cell becomes green in ultrasonic images after extending heating time to 1.5 h, and the interfacial resistance decreases from 0.72 to 0.17 k Ω (**Fig. 4d**).

Long-term electrochemical stability at the PLLZ@HP/Li interface

To further investigate the long-term interfacial evolution process, ultrasonic imaging is carried out during the galvanostatic cycling of the Li/PLLZ@HP/Li pouch cell. The applied current density is set to 0.1 mA cm^{-2} and the operation temperature is fixed at 45 °C. The pouch cell shows no gas release and can be continuously cycled for 500 h without short circuit (**Supplementary Fig. 6 and Fig. 5a**). However, the overpotential decreases first then gradually increases, indicating the dynamic interfacial evolving during the cycling. **Fig. 5b** shows that the overpotential of the Li/PLLZ@HP/Li cell decreases from 0.33 to 0.19 V after the first 40 cycles. Previous studies attributed it to the interfacial activation process, where the interfacial contacts are improved during the initial cycling (**Fig. 5e**)^{29,30}. The ultrasonic images can further vividly confirm this interfacial activation process. The green region of the ultrasonic image before cycling corresponds to the wetted part at the PLLZ@HP/Li interface, while the blue region corresponds to the unwetted part with interfacial voids. As shown in **Fig. 5d**, the blue region gradually disappears after 40 cycles, confirming the enhancement of interfacial contacts. During the following cycling to 500 cycles, the Li/PLLZ@HP/Li cell shows a gradual increase in overpotential from 0.19 to 0.24 V (**Fig. 5c**). Previous studies proposed two possible mechanism for the increased overpotential (**Fig. 5g**). One is the newly generated loss of contacts induced by the dramatic volumetric change of Li anode³¹. The other is the growth of the passivation layer at the interface, which leads to the sluggish Li^+ transport³². Ultrasonic images show that no blue area corresponding to the interfacial voids is generated from 100 cycles to 500 cycles, indicating that the physical contacts are well-maintained after the activation process (**Fig. 5f**). This could be attributed to the excellent flexibility of the PLLZ@HP film, which can efficiently relieve the

interfacial stress and retains the stable interface upon cycling^{33,34}. Therefore, we posit that the increase of overpotential results from the later one, *i.e.*, the growth of a passivation layer.

XPS is then used to analyze the components of the interfacial passivation layer. **Fig. 5h** and **5i** shows the XPS C 1s and O 1s spectra of the PLLZ@HP SSE before and after cycling. The peaks at 284.6 and 286.5 eV in the C 1s spectrum correspond to the C-C and C-O group, respectively¹⁵. An additional peak of O-C=O at 288.8 eV is obtained after cycling, indicative of the oxidized decomposition of the PEO polymer chains³⁵. O 1s spectrum shows the decomposition of the LiTFSI in the passivation layer, where the peaks of O-F_x and Li₂O are observed. FT-IR spectrum further confirms the electrochemical decomposition of the PEO polymer (**Fig. 5j**)³⁶. The chemical components in the passivation layer were recently studied by the cryo-TEM and DFT-based modeling, which agrees with our XPS, FT-IR, and ultrasonic results^{37,38}.

In addition, both the applied current density and capacity of galvanostatic cycling are doubled to 0.2 mA cm⁻² and 0.1 mAh cm⁻², respectively. The cell shows the similar processes of the interfacial activation and the interfacial aging compared with the cell cycled at a low current density (**Supplementary Fig. 7**). A strong ultrasonic transmission signal is obtained even after the short circuit, further confirming excellent interfacial contacts without formation of interfacial voids. Similar to the SEI in the liquid-electrolyte-based batteries, the passivation layer tends to be broken and continuously reacts with the fresh Li metal, thus leading to the Li dendrite growth³⁹. SEM images show a smooth Li metal surface before cycling, while a roughened Li surface with many mossy Li dendrites is observed after cycling (**Supplementary Fig. 8**).

Evaluating the electrochemical window of SSE by ultrasonic imaging

Ultrasonic imaging was also applied to study the interfacial stability at the cathode side. The electrochemical stability window is a critical parameter for SSEs³². High anodic stability of SSE enables the use of high-voltage cathode, and thus raises the energy density. In previous studies, linear sweep voltammetry (LSV) was commonly used to estimate the electrochemical window of the SSEs⁴⁰. However, LSV cannot reflect the relationship between the anodic current and the decomposition mechanism of SSEs. Herein, ultrasonic imaging is carried out to evaluate the decomposition and gas release of the PLLZ@HP during the LSV scan. The inflection point is defined as the onset oxidation voltage. As shown in **Fig. 6a**, the onset oxidation voltage of the PLLZ@HP is ~4.6 V. However, the anodic current of the LSV scan gradually increases from 3.8 to 4.6 V, indicating the initial oxidation below the stability voltage of 4.6 V. The ultrasonic image at 3.8 V shows a relatively homogenous area with green color, which corresponds to the excellent seal and interfacial contacts. The following ultrasonic images at 4.0, 4.2, and 4.4 V exhibit no obvious changes compared with the image taken at 3.8 V. Therefore, the slightly increased anodic current can be attributed to the decomposition of the polymer segments of PLLZ@HP. Interestingly, there is still no gas release at this stage. FT-IR spectrum shows enhanced intensity of the C-H group when the scan voltage increases from 3.8 to 4.4 V, further confirming the decomposition of polymer chains (**Supplementary Fig. 9**). Subsequently, beyond 4.6 V, anodic current goes up rapidly. Correspondingly, the ultrasonic image shows a small blue area at 4.6 V, indicative of gasification. Then,

the enlarging blue areas in the ultrasonic images suggest that gasification progressively intensifies as the scan voltage increases from 4.6 to 5 V. FT-IR spectrum at 5 V shows an additional peak of the O-C=O group compared with the FT-IR spectrum at 4.4 V (**Supplementary Fig. 9**), which indicates that the gas observed in ultrasonic image is due to the further oxidation of polymer segments.

Analyzing failure mechanism at the LCO/SSE cathode interface by ultrasonic imaging

The ultrasonic study of the anodic behavior of the SSE at the cathode interface helps understand the failure mechanism of SSB full cells. Ultrasonic imaging is conducted on a LiCoO₂ (LCO)/PLLZ@HP/Li pouch cell during cycling at 45 °C. The potential range of the galvanostatic stage is set between 2.4 and 4.2 V, and the subsequent constant voltage stage is set at 4.2 V for 1 h. Ultrasonic image at 3.8 V shows relatively uniform green color, indicating the stable interface (**Fig. 6b**). A small blue area appears, which is enclaved in the overall green region when the LCO/PLLZ@HP/Li cell is charged to 4.2 V (**Fig. 6b**). The blue area corresponds to the gas-filled region inside the pouch cell and is slightly enlarged during the potentiostatic process at 4.2 V. Such gassing process is clearer in differential ultrasonic images (**Supplementary Fig. 10**). DEMS analysis shows that the majority of gas released is CO₂ (**Fig. 6c**). XPS results further indicate that the SSE is firstly oxidized to segments with O-C=O groups and then oxidized to CO₂ (**Supplementary Fig. 11**).

The LCO/PLLZ@HP/Li cell delivers a specific discharge capacity of 105.2 mAh g⁻¹ after the first cycle at 0.1 C. The capacity retention is 52.6% after 10 cycles (**Fig. 6d**). Such a poor cycling performance is also reported in recent reports^{41,42}. Although LCO cathode shows excellent electrochemical stability in liquid-based electrolytes, Co element can catalyze the decomposition and gassing of the PLLZ@HP electrolyte at a relative low voltage of 4.2 V^{41,42}. The blue region in the ultrasonic images gradually increases during cycling, indicating the gas accumulation inside the cell (**Fig. 6f**). Such gas accumulation not only hinders ionic transfer, but also brings uneven current distribution in following cycles, which deteriorates of the interface. As shown in **Fig. 6e**, the total resistance of the LCO/PLLZ@HP/Li cell increases from 0.92 to 3.05 kΩ after 10 cycles. Accordingly, surface coating of LCO particles and antioxidative SSEs are potentially helpful to prevent interfacial decomposition and improve the performance of LCO-based SSBs.

Conclusions

Ultrasonic imaging technology is demonstrated as a powerful tool to investigate the interfacial stability in solid-state pouch cells. Ultrasound attenuates significantly when it passes through gasses or voids, and thus is highly sensitive to the quality of interfacial contacts and side reactions. With this method, the stability between the Li metal and PLLZ films with different preparation processes is compared. PLLZ@BC is found to be unstable with the Li metal, due to gas releasing resulted from side-reactions between residual ACN and Li. In contrast, solvent-free PLLZ@HP is stable with Li metal. According to ultrasonic images, no gassing is detected, and the interfacial contacts are even improved during the first few cycles of a Li/PLLZ@HP/Li symmetric cell, which vividly confirms the activation process surmised in

previous researches. The slow increase of the overpotential in the subsequent long-term cycling is due to the passivation layer growth, rather than the interfacial voids induced by the contact loss. On the other hand, oxidation at the cathode side in SSB is also detected with ultrasonic imaging. The SSE/LCO interface is found to be unstable at 4.2 V vs Li⁺/Li. Trace amount of gas is detected in ultrasonic images, which explains the internal resistance raising and rapid capacity decaying in the solid-state LCO/Li pouch cells. Overall, ultrasonic imaging unites the advantage of intactness, high-sensitivity, fast scanning rate, and excellent compatibility with electrochemical measurements. It is an illustrative method for constructing next-generation SSBs with high energy density and safety.

Methods

Fabrication of the PLLZ@BC

PEO ($M_v = 6 \times 10^5 \text{ g mol}^{-1}$, Aladdin) was dried at 60 °C overnight under vacuum prior to the electrolyte fabrication. Li_{6.4}La₃Zr_{1.4}Ta_{0.6}O₁₂ (LLZTO) ceramic powders were prepared by the solid-state reaction and crushed by planetary high-energy ball-milling to decrease the particle size from 5 μm to 200 nm⁴³. 20 wt% LLZTO particles were added into ACN (15 mL) and dispersed by sonication to improve the dispersion. After that, PEO and LiTFSI (EO/Li⁺ = 12:1 by mol) were added into the solution and stirred continuously for 8 h. Then, the homogenized colloidal solution was cast onto a glass plate with a controlled thickness. The ACN solvent was evaporated in a vacuum oven at 60 °C for 12 h. The thickness of the PLLZ@BC was approximately 100 μm.

Fabrication of the PLLZ@HP

LLZTO powders, PEO, and LiTFSI were homogeneously mixed and ground in a mortar to obtain a small ball. The EO to Li molar ratio was 12:1 and the content of LLZTO powders was 20 wt%. Subsequently, the small ball was sandwiched between two pieces of polytetrafluoroethylene (PTFE) plates and transferred into a vacuum oven. By pressing for 2 h at 100 °C under 20 MPa, a uniform composite electrolyte membrane with the thickness of approximately 100 μm was successfully fabricated.

Characterizations of material properties

Surface and cross-section morphologies of composite electrolytes were investigated by scanning electron microscopy (SEM, S3400). Thermogravimetric analysis (TGA) was tested from 30 to 500 °C at 10 °C min⁻¹ under Ar atmosphere. Fourier transform infrared (FTIR) spectroscopy was conducted using a Bruker Alpha system with a Diamond attenuated total reflection (ATR) window in the range of 4000 to 400 cm⁻¹ at a resolution of 4 cm⁻¹. X-ray photoelectron spectroscopy (XPS, ESCALAB-250) measurements were performed to characterize composition of composite electrolytes before and after cycling.

Electrochemical Performance Tests

The ionic conductivities of the composite electrolytes were measured by the NOVOCONTROL spectrometer fitted with a temperature control system with the frequency range from 0.01 Hz to 40 MHz. The electrolytes were sandwiched between two stainless steels (SS), which were used as the block electrodes. The ionic conductivity σ was calculated based on the following equation:

$$\sigma = \frac{t}{RA} \quad (1)$$

Where t represents the thickness of the electrolyte membrane, R is the bulk resistance of electrolytes, and A refers to the contact area between electrolytes and electrodes. Electrochemical impedance spectroscopy (EIS) measurements were performed in a frequency range from 1 MHz to 0.1 Hz with an amplitude of 10 mV by an Autolab instrument. Galvanostatic cycling tests were conducted using a NEWARE battery cycler (CT-4000) using different current densities at 45 °C. The electrochemical window was examined by SS/electrolyte/Li cells, using linear sweep voltammetry (LSV), which was conducted from 2 V to 5.5 V at a scan rate of 10 mV s⁻¹ by Arbin BT-2000.

Differential electrochemical mass spectrometry (DEMS) was used to test the gas produced by the chemical decomposition of the composite electrolytes, the gas produced of Li/Li symmetric cells and LiCoO₂/Li cells using a customized Swagelok battery mold for testing. Mass signals m/z 2, 4, 16, 28, 30 correspond to H₂, He, CH₄, C₂H₄, C₂H₆.

The composite cathode was prepared as follows: LiCoO₂ was mixed with PEO, PVDF, super P conductive carbon (SP) and LiTFSI in 1-methyl-2-pyrrolidinone (NMP, anhydrous, 99.5%) under vigorous agitation. The homogenized suspension was then casted on a carbon-coated Al foil with a doctor blade, followed by drying at 55 °C for 6 h in air and in vacuum condition at 100 °C for 6 h. The mass ratio of LiCoO₂: SP: PEO: PVDF was 75: 10: 10: 5 by weight and the amount of LiTFSI was based on the content of PEO (EO/Li = 12: 1). The LCO loading is approximately 2 mg cm⁻².

Ultrasonic imaging

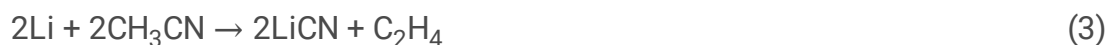
To capture the ultrasonic image, ultrasonic battery scanner (USBC-LD50, from Jiangsu Jitri-Hust Intelligent Equipment Technology Co., Ltd) was applied to accomplish the test. USBC-LD50 main consists of acoustic medium module, motion module and data acquisition module. Pouch cell was fixed in the low-viscosity silicone oil (PMX-200, 10 cSt, Dow Corning Co., Ltd) bath, which connect to the battery test equipment (CT-4008T, Neware Technology Co., Ltd). Two focusing transducers (2 MHz frequency, 40 mm focal distance, focusing diameter <1 mm, customized from Shantou Institute of Ultrasonic Instruments Co., Ltd.) were put on both sides of cell to transmit and receive ultrasonic waves. The motion module could provide an exquisite scanning in horizontal and vertical directions with an optimal precision of 0.1 mm. In this work, 0.2 mm precision was chosen to perform the experiment which takes about 180 s to finish a 25 mm × 30 mm scale scanning. For matching the 2 MHz frequency transducers, a 200 V impulse with 250 ns width as the driving signal. Each transmitted signal during scanning could be

gathered by data acquisition card and transform into a waveform with a peak-to-peak value (PPV) eigenvalue. Further, PPV was converted into a color scale to make the pseudo color image. To evaluate the sensitivity of the ultrasonic imaging, 3 μL gas was generated in the pouch cell by the thermal decomposition of Azobisisobutyronitrile (AIBN) at 85 $^{\circ}\text{C}$. Such small amount of gas can be well reflected in the ultrasonic image (**Supplementary Fig. 12**). It is estimated that 6 μm void/gap is detectable according to the gas area, thus showing a good sensitivity.

DFT calculations

DFT calculations were carried out by the modules DMol3^{44,45} and CASTEP⁴⁶ in Materials Studio 2017. B3LYP functional in Dmol³ module was used to calculate the geometry optimization, energies of the highest and lowest occupied molecular orbitals (HOMO and LUMO). Geometry optimizations were obtained until the maximum force values are less than 0.002 Ha/Å and the maximal atomic displacement is less than 5.0e-3 Å. Core treatment is all-electron using a fine integration grid. Stable self-consistent field (SCF) solutions were obtained, and all structures were optimized. The basis set was DNP (double numerical plus polarization) and the basis file was 3.5.

In CASTEP module calculation, the reaction energies of reactions (2-4) were obtained from the subtraction of total energy of reactants from that of resultants. Total energies of each reactant and resultant were calculated through periodic boundary conditions (PBC) after each single molecule is put into a 20.0 Å cubic unit cell. The generalized gradient approximation (GGA) within Perdew, Burke and Ernzerhof (PBE) is used for exchange-correlation energy. We choose ultrasoft pseudopotential as the core electrons treatment and Broyden–Fletcher–Goldfarb–Shanno (BFGS) scheme as the minimization algorithm respectively. And the valence electron functions were expanded into a set of numerical atomic orbitals using DNP. Geometry optimizations were employed until the maximal energy change per atom is less than 1.0e⁻⁵ eV. The maximal force on the atoms was less than 0.03 eV Å⁻¹. The maximal stress was less than 0.05 and the maximal atomic displacement was less than 1.0e⁻³ Å. The energy cutoff was set to as 500 eV and Monkhorst-Pack k-point mesh was 1 × 1 × 1.



The reaction energy (ΔE) was calculated using the equation:

$$\Delta E = E_{\text{resultants}} - E_{\text{reactants}}$$

$\Delta E < 0$ indicates that the reaction is an exothermic process and thermodynamically feasible.

Declarations

Funding: the authors thank the financial support from National Key R&D Program of China (2018YFB0905400), National Natural Science Foundation of China (51802224 and 21975186) and “Shanghai Rising-Star Program” (19QA1409300).

Author contributions: H. H. conceived and designed the experimental work and prepared the manuscript; K. H. and Z. D. carried out the ultrasonic imaging; J. M. carried out the DFT simulations; H. H. and J. W. fabricated the solid-state pouch cells; L. Z. and Z. H. helped with the DEMS tests; X. G. provided the LLZTO powder. Y. D. drew the schematic. X. J. edited the manuscript. Y. S. designed the ultrasonic imaging experiments. W. L. and Y. H. supervised the overall project. All authors have given approval to the final version of the manuscript.

Competing interests: the authors declare no competing interests.

Data and materials availability: All data are available in the main text or the supplementary materials. Additional data related to this paper may be requested from the authors.

References

- 1 Tarascon, J.-M. & Armand, M. Issues and challenges facing rechargeable lithium batteries. *Nature* **414**, 359-367 (2001).
- 2 Armand, M. & Tarascon, J.-M. Building better batteries. *Nature* **451**, 652-657 (2008).
- 3 Krauskopf, T., Richter, F. H., Zeier, W. G. & Janek, J. Physicochemical Concepts of the Lithium Metal Anode in Solid-State Batteries. *Chem. Rev.* **120**, 7745-7794, doi:10.1021/acs.chemrev.0c00431 (2020).
- 4 Wang, C. *et al.* Garnet-Type Solid-State Electrolytes: Materials, Interfaces, and Batteries. *Chem. Rev.* **120**, 4257-4300, doi:10.1021/acs.chemrev.9b00427 (2020).
- 5 Randau, S. *et al.* Benchmarking the performance of all-solid-state lithium batteries. *Nature Energy*, 1-12 (2020).
- 6 Chen, Y. *et al.* Li metal deposition and stripping in a solid-state battery via Coble creep. *Nature* **578**, 251-255 (2020).
- 7 Zhao, Q., Stalin, S., Zhao, C.-Z. & Archer, L. A. Designing solid-state electrolytes for safe, energy-dense batteries. *Nature Reviews Mater.* **5**, 229-252 (2020).
- 8 Xu, K. Electrolytes and interphases in Li-ion batteries and beyond. *Chem. Rev.* **114**, 11503-11618 (2014).
- 9 Banerjee, A., Wang, X., Fang, C., Wu, E. A. & Meng, Y. S. Interfaces and interphases in All-Solid-State batteries with inorganic solid electrolytes. *Chem. Rev.* **120**, 6878-6933 (2020).

- 10 Xiao, Y. *et al.* Understanding interface stability in solid-state batteries. *Nature Reviews Mater.* **5**, 105-126, doi:10.1038/s41578-019-0157-5 (2019).
- 11 Lim, H.-D. *et al.* A review of challenges and issues concerning interfaces for all-solid-state batteries. *Energy Storage Mater.* **25**, 224-250, doi:10.1016/j.ensm.2019.10.011 (2020).
- 12 Wu, J., Liu, S., Han, F., Yao, X. & Wang, C. Lithium/Sulfide All-Solid-State Batteries using Sulfide Electrolytes. *Adv. Mater.*, e2000751, doi:10.1002/adma.202000751 (2020).
- 13 Han, X. *et al.* Negating interfacial impedance in garnet-based solid-state Li metal batteries. *Nat. Mater.* **16**, 572-579, doi:10.1038/nmat4821 (2017).
- 14 Luo, W. *et al.* Transition from Superlithiophobicity to Superlithiophilicity of Garnet Solid-State Electrolyte. *J. Am. Chem. Soc.* **138**, 12258-12262, doi:10.1021/jacs.6b06777 (2016).
- 15 Huo, H. *et al.* In-situ formed Li₂CO₃-free garnet/Li interface by rapid acid treatment for dendrite-free solid-state batteries. *Nano Energy* **61**, 119-125, doi:10.1016/j.nanoen.2019.04.058 (2019).
- 16 Xiang, Y., Li, X., Cheng, Y., Sun, X. & Yang, Y. Advanced characterization techniques for solid state lithium battery research. *Mater. Today* **36**, 139-157, doi:10.1016/j.mattod.2020.01.018 (2020).
- 17 Knehr, K. W. *et al.* Understanding full-cell evolution and non-chemical electrode crosstalk of li-ion batteries. *Joule* **2**, 1146-1159 (2018).
- 18 Chang, W. *et al.* Understanding adverse effects of temperature shifts on Li-Ion batteries: an operando acoustic study. *J. Electrochem. Soc.* **167**, 090503 (2020).
- 19 Liu, H. *et al.* Photoacoustic imaging of lithium metal batteries. *ACS Applied Energy Mater.* **3**, 1260-1264 (2019).
- 20 Ladpli, P., Kopsaftopoulos, F., Nardari, R. & Chang, F.-K. in *Smart Materials and Nondestructive Evaluation for Energy Systems 2017*. 1017108 (International Society for Optics and Photonics).
- 21 Gold, L. *et al.* Probing lithium-ion batteries' state-of-charge using ultrasonic transmission—Concept and laboratory testing. *J. Power Sources* **343**, 536-544 (2017).
- 22 Cheng, M. *et al.* Elevated-Temperature 3D Printing of Hybrid Solid-State Electrolyte for Li-Ion Batteries. *Adv. Mater.*, 1800615, doi:10.1002/adma.201800615 (2018).
- 23 Chen, L. *et al.* PEO/garnet composite electrolytes for solid-state lithium batteries: From “ceramic-in-polymer” to “polymer-in-ceramic”. *Nano Energy* **46**, 176-184, doi:10.1016/j.nanoen.2017.12.037 (2018).
- 24 Deng, Z. *et al.* Recent Progress on Advanced Imaging Techniques for Lithium-Ion Batteries. *Adv. Energy Mater.* 2000806, doi:10.1002/aenm.202000806 (2020).

- 25 Kinsler, L. E., Frey, A. R., Coppens, A. B. & Sanders, J. V. *Fundamentals of acoustics*. (1999).
- 26 Xue, Z., He, D. & Xie, X. Poly(ethylene oxide)-based electrolytes for lithium-ion batteries. *J. Mater. Chem. A* **3**, 19218-19253, doi:10.1039/c5ta03471j (2015).
- 27 Huang, C., Leung, C. L. A., Leung, P. & Grant, P. S. A Solid-State Battery Cathode with a Polymer Composite Electrolyte and Low Tortuosity Microstructure by Directional Freezing and Polymerization. *Adv. Energy Mater.* 2002387, doi:10.1002/aenm.202002387 (2020).
- 28 Huo, H. Y. *et al.* Anion-immobilized polymer electrolyte achieved by cationic metal-organic framework filler for dendrite-free solid-state batteries. *Energy Storage Mater.* **18**, 59-67, doi:10.1016/j.ensm.2019.01.007 (2019).
- 29 Huo, H. *et al.* Rational Design of Hierarchical “Ceramic-in-Polymer” and “Polymer-in-Ceramic” Electrolytes for Dendrite-Free Solid-State Batteries. *Advanced Energy Mater.* **9**, 1804004, doi:10.1002/aenm.201804004 (2019).
- 30 Zhang, J. *et al.* Flexible and ion-conducting membrane electrolytes for solid-state lithium batteries: Dispersion of garnet nanoparticles in insulating polyethylene oxide. *Nano Energy* **28**, 447-454, doi:10.1016/j.nanoen.2016.09.002 (2016).
- 31 Kasemchainan, J. *et al.* Critical stripping current leads to dendrite formation on plating in lithium anode solid electrolyte cells. *Nat. Mater.* **18**, 1105-1111, doi:10.1038/s41563-019-0438-9 (2019).
- 32 Zhou, D., Shanmukaraj, D., Tkacheva, A., Armand, M. & Wang, G. Polymer Electrolytes for Lithium-Based Batteries: Advances and Prospects. *Chem* **5**, 2326-2352, doi:10.1016/j.chempr.2019.05.009 (2019).
- 33 Shao, Y. *et al.* Drawing a Soft Interface: An Effective Interfacial Modification Strategy for Garnet-Type Solid-State Li Batteries. *ACS Energy Lett.* **3**, 1212-1218 (2018).
- 34 Huo, H. *et al.* A flexible electron-blocking interfacial shield for dendrite-free solid lithium metal batteries. *Nat. Commun.* **12**, 176, doi:10.1038/s41467-020-20463-y (2021).
- 35 Liang, J. *et al.* Stabilizing and understanding the interface between nickel-rich cathode and PEO-based electrolyte by lithium niobium oxide coating for high-performance all-solid-state batteries. *Nano Energy* **78**, 105107, doi:10.1016/j.nanoen.2020.105107 (2020).
- 36 Xu, Q. *et al.* The photocatalytic degradation of chloramphenicol with electrospun Bi₂O₂CO₃-poly(ethylene oxide) nanofibers: the synthesis of crosslinked polymer, degradation kinetics, mechanism and cytotoxicity. *RSC Advances* **9**, 29917-29926, doi:10.1039/c9ra06346c (2019).
- 37 Sheng, O. *et al.* In Situ Construction of a LiF-Enriched Interface for Stable All-Solid-State Batteries and its Origin Revealed by Cryo-TEM. *Adv. Mater.* **32**, e2000223, doi:10.1002/adma.202000223 (2020).

- 38 Mirsakiyeva, A. *et al.* Initial Steps in PEO Decomposition on a Li Metal Electrode. *J. Phys. Chem. C* **123**, 22851-22857, doi:10.1021/acs.jpcc.9b07712 (2019).
- 39 Cheng, X. B., Zhang, R., Zhao, C. Z. & Zhang, Q. Toward Safe Lithium Metal Anode in Rechargeable Batteries: A Review. *Chem. Rev.* **117**, 10403-10473, doi:10.1021/acs.chemrev.7b00115 (2017).
- 40 Marchiori, C. F. N., Carvalho, R. P., Ebadi, M., Brandell, D. & Araujo, C. M. Understanding the Electrochemical Stability Window of Polymer Electrolytes in Solid-State Batteries from Atomic-Scale Modeling: The Role of Li-Ion Salts. *Chem. Mater.* **32**, 7237-7246, doi:10.1021/acs.chemmater.0c01489 (2020).
- 41 Wang, Y. *et al.* An In Situ Formed Surface Coating Layer Enabling LiCoO₂ with Stable 4.6 V High Voltage Cycle Performances. *Adv. Energy Mater.* **10**, 2001413, doi:10.1002/aenm.202001413 (2020).
- 42 Qiu, J. *et al.* Enabling Stable Cycling of 4.2 V High-Voltage All-Solid-State Batteries with PEO-Based Solid Electrolyte. *Adv. Funct. Mater.* **30**, 1909392, doi:10.1002/adfm.201909392 (2020).
- 43 Li, Y., Cao, Y. & Guo, X. Influence of lithium oxide additives on densification and ionic conductivity of garnet-type Li_{6.75}La₃Zr_{1.75}Ta_{0.25}O₁₂ solid electrolytes. *Solid State Ionics* **253**, 76-80 (2013).
- 44 Delley, B. An all-electron numerical method for solving the local density functional for polyatomic molecules. *J. Chem. Phys.* **92**, 508-517 (1990).
- 45 Delley, B. From molecules to solids with the DMol 3 approach. *J. Chem. Phys.* **113**, 7756-7764 (2000).
- 46 Clark, S. J. *et al.* First principles methods using CASTEP. *Zeitschrift für Kristallographie-Crystalline Mater.* **220**, 567-570 (2005).

Figures

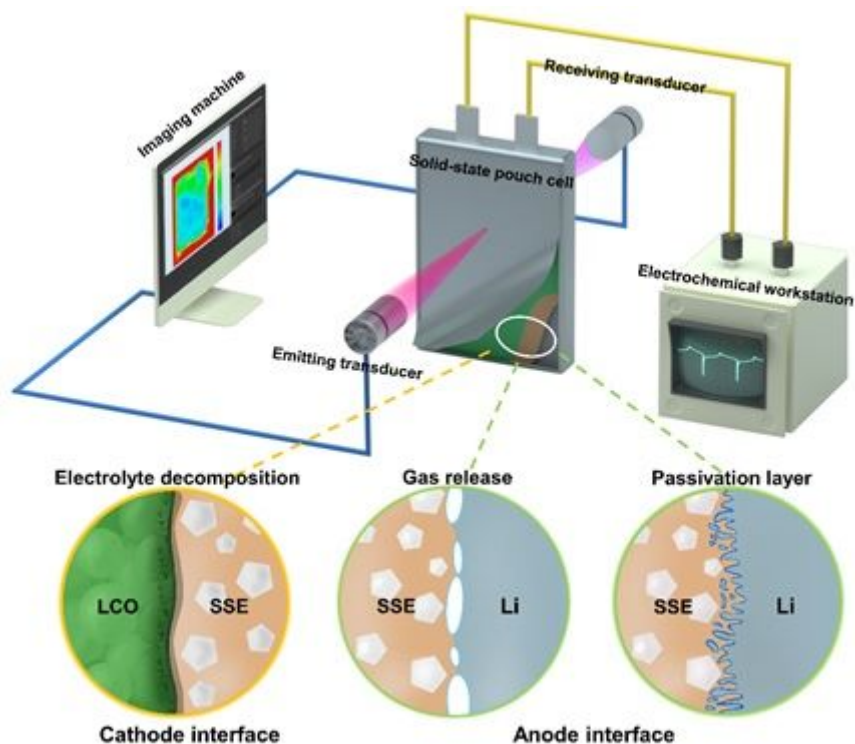


Figure 1

Schematic of the ultrasonic imaging. A schematic diagram of the ultrasonic imaging technique to study the interfaces in SSBs.

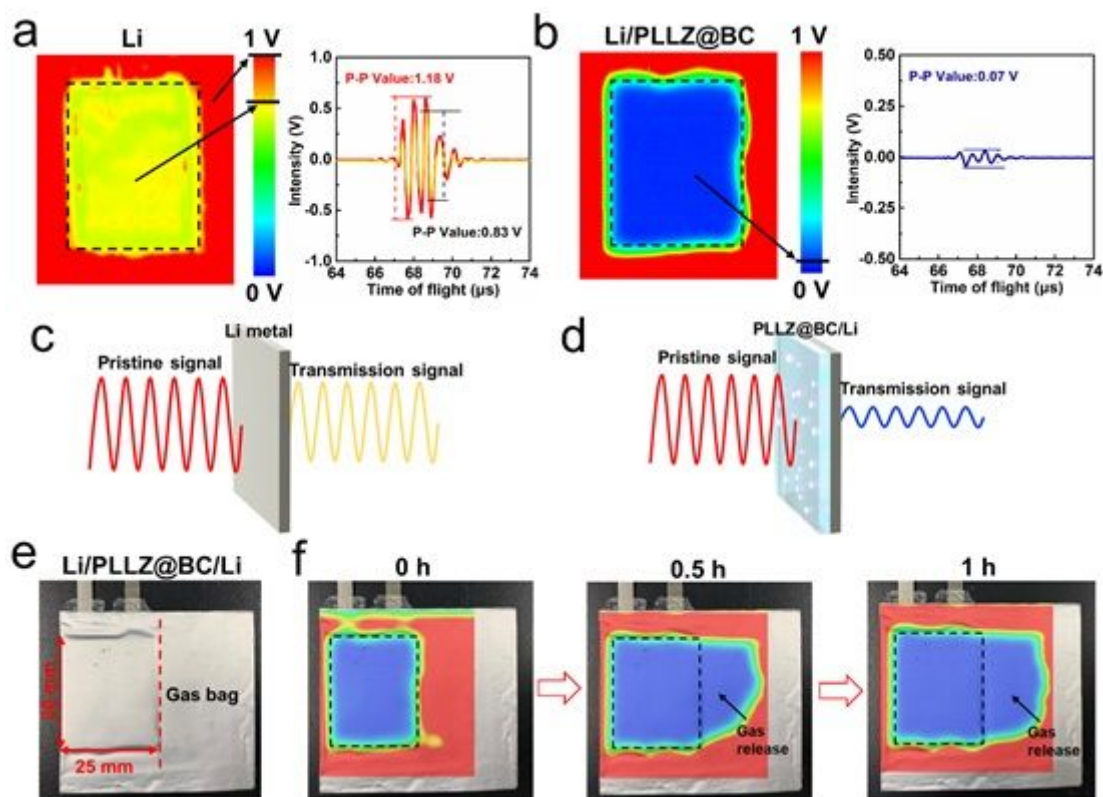


Figure 2

Gassing detection in the Li/PLLZ@BC/Li pouch cell. (a) The ultrasonic transmission image of the Li metal and the ultrasonic waves at the position marked by the arrows. (b) The ultrasonic transmission image of the PLLZ@BC/Li and the ultrasonic wave at the position marked by the arrow. Schematic images of the PLLZ@BC/Li and the ultrasonic signal passing through (c) the Li metal and (d) the PLLZ@BC/Li. (e, f) A photograph of a Li/PLLZ@BC/Li pouch cell and corresponding ultrasonic transmission images of the cell overlapped on its optical photo after storing for 0, 0.5, and 1 h, respectively.

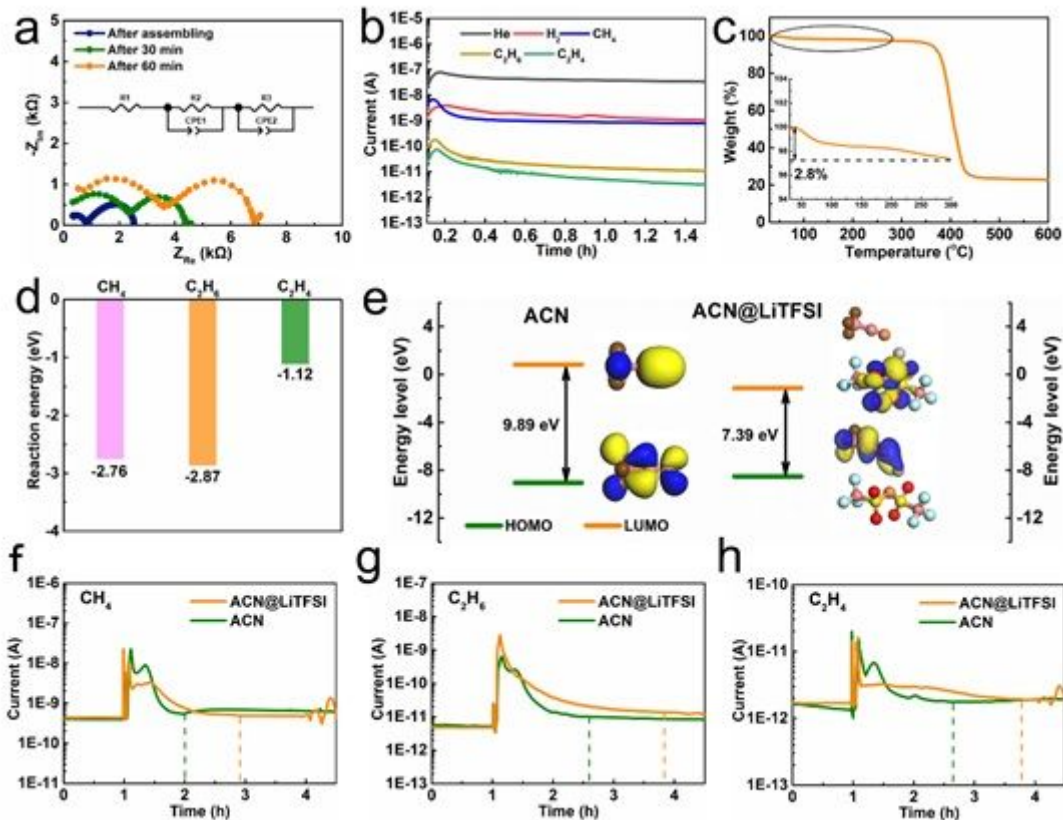


Figure 3

Gas species and source in the Li/PLLZ@BC/Li pouch cell. (a) EIS spectra of the Li/PLLZ@BC/Li cell right after assembling, after 30 min, and 60 min. (b) DEMS results for the Li/PLLZ@BC/Li cell at open circuit. (c) TGA curve of the PLLZ@BC electrolyte. (d) Calculated reaction energy of gases by the reactions between the ACN and the Li metal. (e) Calculated HOMO and LUMO of ACN, and ACN@LiTFSI with the molecular structure, respectively. DEMS results of (f) CH₄, (g) C₂H₆, and (h) C₂H₄ in the Li/ACN@LiTFSI/Li and Li/ACN/Li cells.

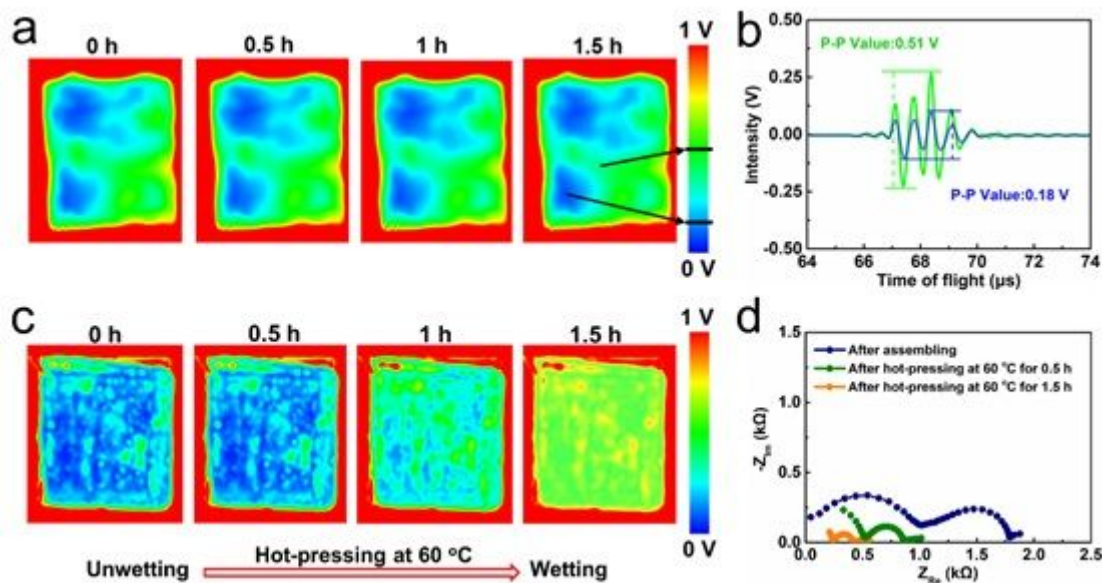


Figure 4

Chemical stability and wetting behavior at the PLLZ@HP/Li interface. (a) The ultrasonic transmission images of the Li/PLLZ@HP/Li cell after different time. (b) The ultrasonic waves at the positions marked by the arrows. (c) The interfacial wetting process of the Li/PLLZ@HP/Li cell during the hot-pressing at 60 °C. (d) EIS spectra of the Li/PLLZ@HP/Li cell after assembling, and after hot-pressing at 60 °C for 0.5 and 1.5 h.

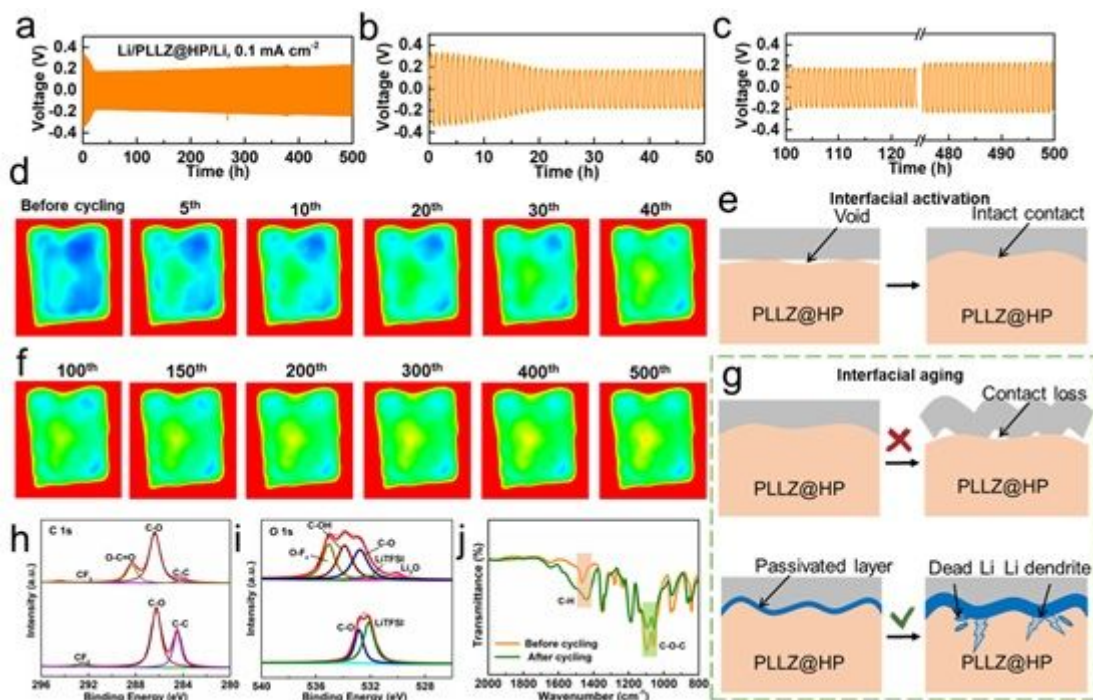


Figure 5

Electrochemical stability at the PLLZ@HP/Li interface. (a) Galvanostatic cycling profiles of the Li/PLLZ@HP/Li cell at 0.1 mA cm⁻² with a capacity of 0.05 mAh cm⁻² at 45 °C. (b, c) Magnified profiles

for the duration of 0-50 h and 100-500 h. (d) The corresponding ultrasonic transmission images of the Li/PLLZ@HP/Li cell during the first 40 cycles. (e) Schematic illustration of the interfacial activation process. (f) The corresponding ultrasonic transmission images of the Li/PLLZ@HP/Li cell during 100-500 cycles. (g) Schematic illustration of a possible mechanism for the increased overpotential. XPS spectra of (h) C 1s and (i) O 1s for the PLLZ@HP before and after cycling. (j) FT-IR spectrum of the PLLZ@HP before and after cycling.

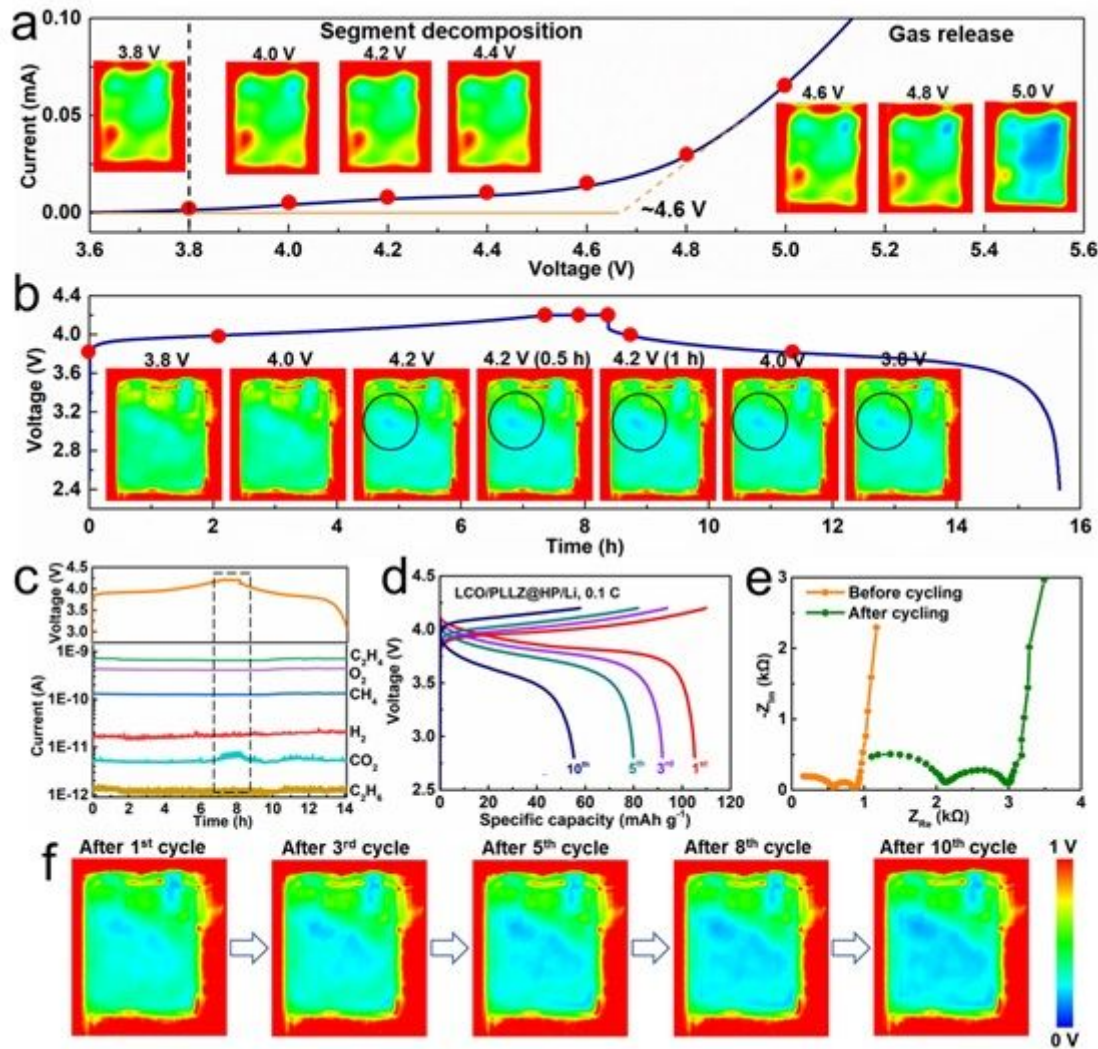


Figure 6

Interfacial degradation at the LCO/SSE interface evaluated by the ultrasonic imaging. (a) Ultrasonic transmission images of the Li/PLLZ@HP/Stainless steel (SS) cell during the LSV scanning. (b) Ultrasonic transmission images of the LCO/PLLZ@HP/Li cell during the cycling at 0.1 C. (c) Voltage profiles and the corresponding DEMS results of the LCO/PLLZ@HP/Li cell cycled at 0.1 C. (d) Charge/discharge profiles of the LCO/PLLZ@HP/Li cell at 0.1 C. (e) EIS spectra of the LCO/PLLZ@HP/Li cell before and after cycling. (f) Ultrasonic transmission images of the LCO/PLLZ@HP/Li cell after different cycles.

Supplementary Files

This is a list of supplementary files associated with this preprint. Click to download.

- [NatureCommunicationsSI.doc](#)
- [NatureCommunicationsSI.doc](#)